nature communications

Article

https://doi.org/10.1038/s41467-024-51826-4

Detection of carbon dioxide and hydrogen peroxide on the stratified surface of Charon with JWST

Received: 15 November 2023

Accepted: 14 August 2024

Published online: 01 October 2024

Check for updates

Silvia Protopapa[1] ✉, Ujjwal Raut[2,3], Ian Wong[4,5,6], John Stansberry[6,7,8], Geronimo L. Villanueva[4], Jason Cook[9], Bryan Holler[6], William M. Grundy[7,8], Rosario Brunetto[10], Richard J. Cartwright[11], Bereket Mamo[2,3], Joshua P. Emery[8], Alex H. Parker[12], Aurelie Guilbert-Lepoutre[13], Noemi Pinilla-Alonso[14], Stefanie N. Milam[4] & Heidi B. Hammel[15]

Charon, Pluto's largest moon, has been extensively studied, with research focusing on its primitive composition and changes due to radiation and photolysis. However, spectral data have so far been limited to wavelengths below 2.5 µm, leaving key aspects unresolved. Here we present the detection of carbon dioxide (CO_2) and hydrogen peroxide (H_2O_2) on the surface of Charon's northern hemisphere, using JWST data. These detections add to the known chemical inventory that includes crystalline water ice, ammonia-bearing species, and tholin-like darkening constituents previously revealed by ground- and space-based observations. The H_2O_2 presence indicates active radiolytic/photolytic processing of the water ice-rich surface by solar ultraviolet and interplanetary medium Lyman-α photons, solar wind, and galactic cosmic rays. Through spectral modeling of the surface, we show that the CO_2 is present in pure crystalline form and, possibly, in intimately mixed states on the surface. Endogenically sourced subsurface CO_2 exposed on the surface is likely the primary source of this component, with possible contributions from irradiation of hydrocarbons mixed with water ice, interfacial radiolysis between carbon deposits and water ice, and the implantation of energetic carbon ions from the solar wind and solar energetic particles.

Charon, Pluto's largest moon, stands unique as the only mid-sized trans-Neptunian object (TNO)—i.e., with a diameter between 500 and 1700 km—for which geological mapping is available, thanks to measurements returned by the New Horizons mission[1,2]. Unlike larger TNOs (e.g., Pluto, Eris, and Makemake), Charon's surface is not obscured by hyper-volatile ices, such as methane (CH_4), with the possible exception toward the poles. As a result, Charon serves as an excellent candidate for retrieving valuable insights into processes such as differentiation, radiation exposure, and cratering within the Kuiper Belt. Understanding how these processes operate in the Kuiper Belt is critical when attempting to deduce the primitive composition of TNOs.

[1]Southwest Research Institute, Boulder, CO, USA. [2]Southwest Research Institute, San Antonio, TX, USA. [3]University of Texas at San Antonio, San Antonio, TX, USA. [4]NASA Goddard Space Flight Center, Greenbelt, MD, USA. [5]American University, Washington, DC, USA. [6]Space Telescope Science Institute, Baltimore, MD, USA. [7]Lowell Observatory, Flagstaff, AZ, USA. [8]Northern Arizona University, Flagstaff, AZ, USA. [9]Pinhead Institute, Telluride, CO, USA. [10]Université Paris-Saclay, CNRS, Institut d'Astrophysique Spatiale, Orsay, France. [11]Johns Hopkins University Applied Physics Laboratory, Laurel, MD, USA. [12]SETI Institute, Mountain View, CA, USA. [13]LGL-TPE, UMR 5276 CNRS, Université Lyon 1, ENS, Villeurbanne, France. [14]Florida Space Institute, University of Central Florida, Orlando, FL, USA. [15]Association of Universities for Research in Astronomy, Washington, DC, USA. ✉e-mail: silvia.protopapa@swri.org

Charon has been the focus of extensive spectral analysis through both ground-based and space-based observations[3–5]. This includes data collected by New Horizons[1,2]. These investigations have uncovered a surface largely composed of crystalline water (H_2O) ice and ammonia (NH_3)-bearing species[6,7]. These compounds exhibit increased concentrations in the bright ejecta blankets surrounding younger craters, suggesting the excavation of subsurface materials[8]. Two darkening agents have been proposed on Charon's surface: one is a highly processed hydrocarbon, presumably originating from Kuiper Belt impactors; the other is a red, tholin-like compound localized at the polar regions, likely resulting from the irradiation of cold-trapped volatiles that migrated from Pluto to Charon[9,10]. Given the limited wavelength coverage of Charon's measurements to date (up to 2.5 μm), some aspects of Charon's composition remain unresolved, including (1) the detection of carbon dioxide (CO_2), expected to be present in regions where subsurface materials are exposed, but never previously detected, and (2) the role of energetic radiation and ultraviolet (UV) photolysis on H_2O ice, ammoniated species, and carbon (C)-bearing species.

Exploring exogenous and endogenous processes requires putting Charon's spectroscopic measurements in context with those of other icy moons in the Solar System and more primitive bodies (e.g., comets). Investigating the surface composition of these bodies can then offer insights into potentially common chemical compounds that might have been present in various regions of the solar nebula, as well as the possible formation of similar radiolytic and/or photolytic by-products on their surfaces.

In this work, we present observations of Charon acquired by the James Webb Space Telescope (JWST) Near-Infrared Spectrograph (NIRSpec[11]), extending beyond 2.5 μm up to 5.2 μm. We report the detection of CO_2 and hydrogen peroxide (H_2O_2) on Charon's frozen surface. Through spectral modeling analysis, comparison with laboratory measurements, and reference to JWST observations of Jupiter's moon Europa[12,13], we investigate the nature and sources of these compounds. Our results highlight insights into the chemical diversity and evolutionary processes on Charon.

Results

The Pluto–Charon system was observed using the JWST/NIRSpec instrument as part of the Cycle 1 Solar System Guaranteed Time Observations (GTO) program #1191. Four observations were obtained at different sub-observer longitudes to provide full coverage of Charon's northern hemisphere. These observations utilized the integral field unit (IFU) on NIRSpec, which has a $3.0'' \times 3.0''$ field of view and a spatial resolution of $0.1''$ per pixel. The high-resolution gratings G140H, G235H, and G395H were employed, which cover the wavelength ranges 1.0–1.8 μm, 1.7–3.1 μm, and 2.9–5.2 μm, respectively, at a spectral resolving power of approximately 2700[11]. The total effective exposure times in the three spectral settings for each of the four visits were 408, 554, and 1109 s, respectively, yielding a combined exposure time of 2072 s per observation (Supplementary Table 1). In Fig. 1, we display the spectra of Charon's full disk at the four sub-observer longitudes, calibrated in units of radiance factor (or equivalently, *I*/*F*), along with the detected surface ice features. The radiance factor is the ratio of the bidirectional reflectance of a surface to that of a perpendicularly illuminated, perfectly diffuse Lambertian surface, where both surfaces are the same size and are at the same distance from the Sun and the observer[14]. Details on data reduction and spectral extraction can be found in the Data Reduction section in the Methods. The Charon spectra, specifically the *I*/*F* level and the depth of the absorption bands, show minimal variation with longitude. The average standard deviation of the mean of the four spectra and across the entire wavelength range is 0.4%. Therefore, we average the four spectra to derive the grand average shown in panel g of Fig. 1. The uncertainties on each data point are represented by the standard deviation of the mean. The grand-average spectrum has an average signal-to-noise ratio of 91, 85, and 10 across the wavelength ranges 1.1–2.4 μm, 3.2–4.0 μm, and 4.2–4.4 μm, respectively. Given the negligible longitudinal variations observed, our analysis will primarily concentrate on Charon's globally averaged spectrum.

The grand-average spectrum of Charon from JWST is shown alongside a disk-averaged spectrum from the New Horizons Linear Etalon Imaging Spectral Array (LEISA) instrument[8] in Fig. 1g. The JWST spectrum aligns well with the New Horizons/LEISA data, particularly in the continuum slope and band profile of the absorption bands at 1.5, 1.65, and 2.0 μm, which have been attributed to crystalline H_2O ice features[3,4] (see Supplementary Fig. 1). This serves as a valuable confirmation of the data reduction methods used for the JWST Charon observations. Discrepancies in the absolute *I*/*F* values between the two data sets can be attributed primarily to the different viewing geometries. Specifically, the New Horizons data were acquired at a mean distance from Charon's center of 80,653 km at an average phase angle of roughly 36°, whereas the JWST data were obtained at a phase angle of around 1.5°. This makes the JWST data particularly sensitive to the "opposition effect"—a steep, nonlinear increase in reflectance observed as phase angles approach zero[15]. JWST/NIRSpec extends the spectral coverage of Charon beyond the 2.5-μm cutoff of New Horizons/LEISA to 5.2 μm. The broader wavelength range has unveiled two species on Charon's icy surface: CO_2 ice and H_2O_2. Furthermore, it offers deeper insights into the overall ice inventory on Charon.

Carbon dioxide detection

CO_2 ice on the surface of Charon is identified by its characteristic absorption features, specifically the $\nu_1 + \nu_3$ combination band near 2.70 μm and the C=O asymmetric stretching fundamental ν_3 at 4.27 μm (Fig. 2a, b).

We modeled the continuum region near 2.7 μm (red line, Fig. 2a) without including a contribution from CO_2, de-weighting the data in the 2.69–2.71 μm range where the absorption band occurs (refer to the "Spectral modeling" section in the Methods for more details). A Lorentzian fit to the continuum-removed combination band displays a sharp, narrow absorption at 2.6966 ± 0.0001 μm with a full width at half maximum (FWHM) of 0.0019 ± 0.0004 μm and a band depth, relative to the continuum, of $32 \pm 4\%$ (Fig. 2c, red solid line). The uncertainties in the FWHM, band center, and band depth parameters were determined using Markov Chain Monte Carlo (MCMC) analysis (Supplementary Fig. 2). For comparison, the JWST spectrum of Europa[12] displays a band with similar characteristics to that of Charon, but with a band depth on the order of 12% (Fig. 2c, cyan points and red dashed line). Spectra of solid CO_2 from various matrix environments, as reported by multiple laboratories, were compared with the CO_2 absorption feature at 2.7 μm observed on Charon, as illustrated in Fig. 2c.

Spectra of pure amorphous CO_2 do not align with Charon's 2.7-μm absorption feature. The $\nu_1 + \nu_3$ band of solid amorphous CO_2 peaks close to 2.70 μm. However, its band center is shifted toward longer wavelengths compared to crystalline CO_2[16]. Additionally, the band profile for the amorphous phase is broader, with an FWHM approximately three times larger than that of its crystalline counterpart[16–18] (see olive dash-dot line in Fig. 2c).

Solid CO_2, when mixed with other constituents, does not yield a close match to Charon's 2.7 μm feature. For instance, irradiation of pure CO_2 ice with 100 keV protons (H^+) results in CO_2 depletion and the accumulation of carbon monoxide (CO), oxygen (O_2), and minor species such as ozone (O_3) and carbon trioxide (CO_3)[19]. The changing matrix environment results in the broadening of the 2.7-μm feature[19], as shown by the pink dashed line in Fig. 2c. Similar considerations apply to CO_2 diluted in H_2O, both in its pure form (olive dashed line in Fig. 2c, with a possible contribution from the dangling bond of solid H_2O[18]) and post irradiation (dark green solid line in

https://doi.org/10.1038/s41467-024-51826-4

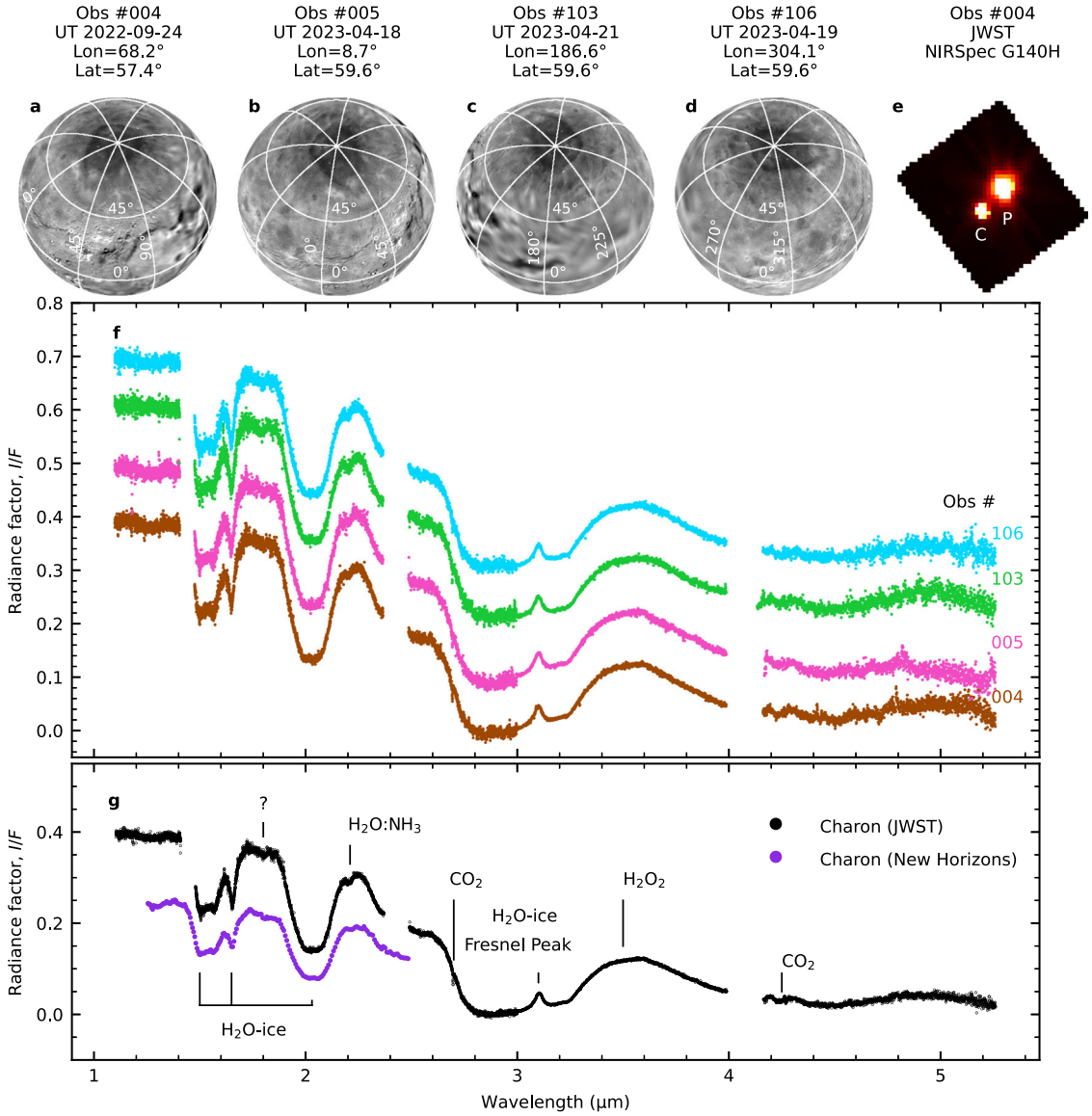

Fig. 1 | JWST/NIRSpec IFU observations of Charon and detected ice species. **a**–**d** Charon's surface, as imaged by the New Horizons/LOng Range Reconnaissance Imager (LORRI) and Multi-spectral Visible Imaging Camera (MVIC) instruments[81,82], is presented in orthographic projection, centered on the sub-observer longitude and latitude during the four JWST observations. **e** Image of Pluto (marked as "P") and Charon (marked as "C"), generated by median-combining all slices within the wavelength range covered by the JWST/NIRSpec IFU G140H grating (observation #004). **f** The *I*/*F* spectra extracted from each observation, offset along the y-axis for clarity. Gaps observed in the extracted Charon spectra arise from a physical separation between the two NIRSpec detectors, NRS1 and NRS2, in the focal plane array. This impacts NIRSpec IFU observations using high-resolution gratings, as the spectra are broad enough to encompass both detectors. **g** The grand-average spectrum of Charon, obtained by averaging all four spectra. The compounds that account for the detected absorption bands in Charon's spectrum are labeled in the figure. All four observations demonstrate consistent spectral shapes, displaying not only H_2O ice absorption bands and the 2.2-μm feature attributed to NH_3 diluted in H_2O ice but also distinct evidence of the CO_2 combination mode at 2.70 μm and the asymmetric stretching fundamental at 4.27 μm, as well as a plateau at 3.5 μm due to H_2O_2. Additionally, an absorption band centered around 1.8 μm is observed, though its nature remains uncertain. For comparison, the disk-averaged spectrum from New Horizons/LEISA's C_LEISA_HIRES scan of Charon[8] is also shown (purple points). Source data are provided as a Source Data file.

Fig. 2c). The observed shift toward longer wavelengths and the broadening of the $\nu_1+\nu_3$ band upon diluting CO_2 in H_2O, as seen in our laboratory data, are consistent with other laboratory studies[20]. For a detailed description of our laboratory experiments on H_2O–CO_2 ice mixtures, the reader is referred to the "Laboratory experiments" section in the Methods. CO_2 mixed with H_2O and methanol (CH_3OH) ices in nearly equal proportions[21], at temperatures relevant to the surface of Charon (approximately 50 K[22]), is inconsistent with the observations. This discrepancy can be seen in the purple dash-dot line of Fig. 2c.

Given these lines of evidence, amorphous CO_2, irradiated CO_2, CO_2 diluted in H_2O, and the three-component mixture of CO_2, CH_3OH, and H_2O ice do not match the band position and profile of the $\nu_1+\nu_3$ band observed in Charon's JWST spectrum. Instead, pure (poly)crystalline CO_2 emerges as the primary contributor, as shown by the blue and cyan solid lines in Fig. 2c[16,18,19,23]. A subtle variation in the $\nu_1+\nu_3$ band position has been observed in laboratory measurements of pure crystalline CO_2[16,19,23], which might be influenced by the CO_2 temperature and/or the sample's degree of crystallinity.

While the $2\nu_2+\nu_3$ combination/overtone band near 2.78 μm is evident in the laboratory spectra of pure crystalline CO_2[16,19,23], it is challenging to identify in Charon's JWST spectra due to the low signal-to-noise ratio in this wavelength region (i.e., $I/F < 10^{-2}$).

https://doi.org/10.1038/s41467-024-51826-4

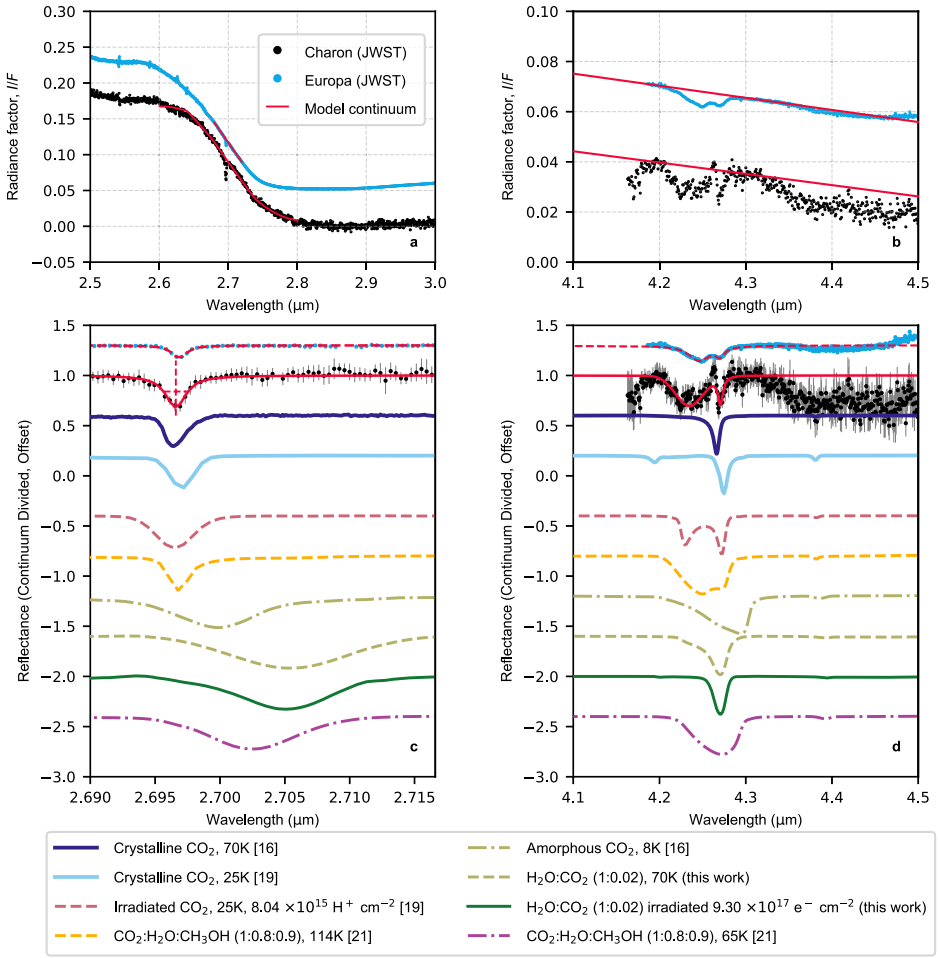

Fig. 2 | The nature of carbon dioxide on the surface of Charon. a, **b** The JWST spectrum of Charon, represented by black points, is displayed in two wavelength regions where the $\nu_1+\nu_3$ and $2\nu_2+\nu_3$ (panel **a**) as well as the ν_3 (panel **b**) CO_2 absorption bands occur. For comparison, the JWST spectrum of Europa[12] is shown (cyan points). The Europa spectrum is normalized to Charon's *I*/*F* level at 2.52–2.54 μm (panel **a**) and 4.28–4.29 μm (panel **b**), and has been vertically shifted for better visualization. The red lines show the model of the local continuum around the CO_2 bands under study (refer to the main text for detailed discussion). **c**, **d** Continuum-corrected spectra of Charon and Europa are shown together with their 1-σ errors. Both the dashed and solid red lines illustrate fits of the CO_2 band profile, which utilizes a combination of Gaussian and Lorentzian profiles. For comparison, colored lines show various types of CO_2 measured in the laboratory. Initially expressed in terms of absorbance (or optical depth), these measurements underwent conversion to reflectance, ensuring the preservation of the original sample thickness. Subsequent continuum correction was applied, followed by scaling to align with the observed band depth. These spectra, while vertically offset, serve as benchmarks for evaluating spectral shape and position. Source data are provided as a Source Data file.

The spectrum of Charon in the wavelength range between 2.66 and 2.80 μm, which includes both the $\nu_1+\nu_3$ and $2\nu_2+\nu_3$ CO_2 absorption bands, was modeled using the Hapke radiative transfer model[14]. Specifically, the best-fit model consists of an areal mixture of 80% crystalline H_2O ice, 18% amorphous H_2O ice, and 2% crystalline CO_2 (for details, refer to the "Spectral modeling" section in the Methods and Supplementary Fig. 3).

We do not find evidence for the absorption bands of solid crystalline CO_2[23] at 1.97 μm ($2\nu_1+\nu_3$), 2.01 μm ($\nu_1+2\nu_2+\nu_3$), and 2.07 μm ($4\nu_2+\nu_3$), consistent with the New Horizons data (Fig. 1g and Supplementary Fig. 1). It is worth noting that, based on absorption coefficient considerations[16], the $\nu_1+\nu_3$ and ν_3 CO_2 absorption bands probe penetration depths on the order of 1 μm and 0.1 μm, respectively. These depths refer to how far into a material the light can penetrate before being absorbed, directly relating to the depth below the surface that is being probed. In contrast, the short wavelength absorption bands (i.e., $2\nu_1+\nu_3$, $\nu_1+2\nu_2+\nu_3$, $4\nu_2+\nu_3$[23]) probe the occurrence of CO_2 at approximate depths of 50 μm for $\nu_1+2\nu_2+\nu_3$, 100 μm for $2\nu_1+\nu_3$, and 300 μm for $4\nu_2+\nu_3$. The probe depths listed for the CO_2 absorption bands are based on measurements of pure CO_2. These depths will differ if CO_2 is dispersed in H_2O ice, as we propose here on Charon based on the modeling of the 2.7-μm range (refer to the "Spectral modeling" section in the Methods). In this context, the values obtained for pure CO_2 represent a lower limit. Nevertheless, when accounting for CO_2 dispersed in H_2O ice, the short wavelength bands near 2 μm will still probe hundreds of microns, contrary to the $\nu_1+\nu_3$ and ν_3 bands that will probe approximately the first 5 and 1 μm, respectively. Therefore, the lack of detection of CO_2 absorption features at short wavelengths near 2 μm implies that this compound is sparse at penetration depths greater than several tens of microns, contrary to the case of the Uranian moons[24] and Triton[25].

Charon presents an intriguing double-peaked absorption band ranging from approximately 4.20 to 4.29 μm. At a first-order approximation, it is possible to decompose the observed spectral profile into two components, one broad Gaussian component centered at 4.2346 ± 0.0008 μm with an FWHM of 0.037 ± 0.002 μm and one sharp Lorentzian component centered at 4.2707 ± 0.0005 μm with an FWHM of 0.007 ± 0.001 μm (Fig. 2d, red solid line). The overall width of this double-lobed feature is consistent with that of pure crystalline CO_2 at 70 K[16,26] (blue solid line in Fig. 2d). However, unlike the JWST

https://doi.org/10.1038/s41467-024-51826-4

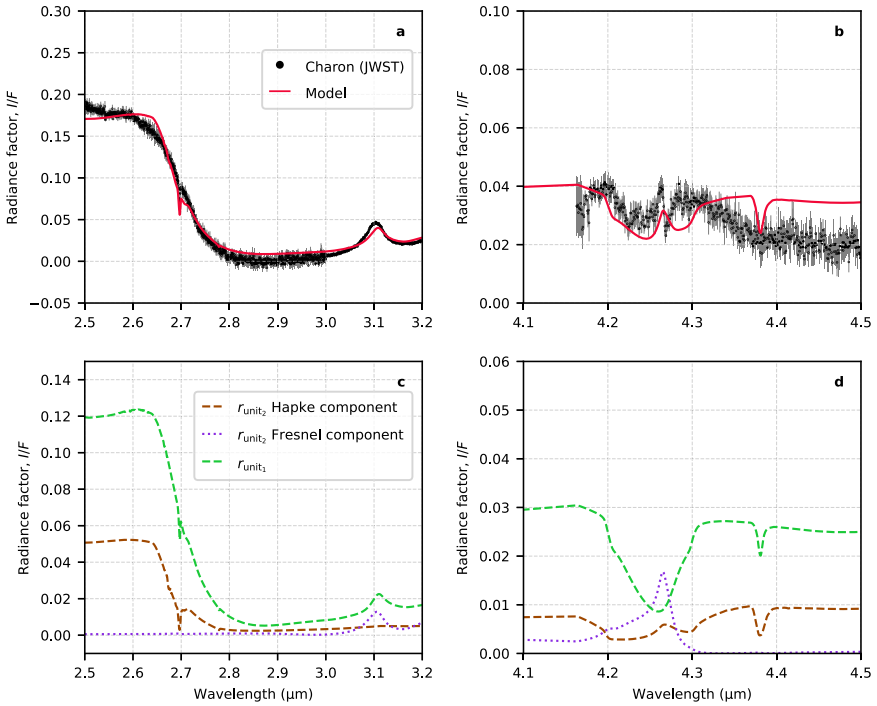

Fig. 3 | Possible CO_2 ice Fresnel peak at 4.265 μm. a, **b** Comparison of the JWST/NIRSpec grand-average spectrum of Charon (black points with 1-σ errors) with a spectral model (red line), which consists of an areal mixture of two surface units (refer to text and "Spectral modeling" section in the Methods for detailed explanation). **c**, **d** The reflectance of each component within the model is shown. The model effectively captures the primary spectral features of Charon's spectrum, though the match is not perfect. The goal of this model is to support the potential interpretation of the 4.265-μm peak as a CO_2 ice Fresnel peak originating from the interface between two layered media, with crystalline CO_2 ice and amorphous H_2O ice on top of a crystalline H_2O ice and tholins layer. Source data are provided as a Source Data file.

spectra, these laboratory data do not exhibit the characteristic dual minima. The data of pure crystalline CO_2 acquired at 25 K[19] exhibit a distinct ν_3 spectral profile compared to those at 70 K[16] and align more closely with the Lorentzian component of the Charon band at 4.27 μm (cyan solid line in Fig. 2d). The reasons for these differences remain unclear at this stage.

The spectrum of H_2O ice containing approximately 2% CO_2 and irradiated to a dose of 10^{18} electrons cm^{-2} at 70 K (dark green solid line in Fig. 2d; see the "Laboratory experiments" section in the Methods for further information) displays a sharp feature at 4.27 μm, resembling the Lorentzian observed in Charon's spectrum. Nonetheless, the exact width of this absorption band and its spectral shape, marked by its symmetric behavior, do not match perfectly the observations. This could imply the presence of CO_2 embedded within H_2O ice that has been modified by irradiation, alongside the naturally occurring pure polycrystalline phase.

The JWST spectrum of Europa also displays a double-peak structure in the same wavelength range[12,13] (cyan points in Fig. 2), though its band distinctly contrasts with the feature in Charon's spectrum. Specifically, the band in the Europa spectrum can be decomposed into two sharp Lorentzian components centered at 4.2462 ± 0.0003 μm and 4.2700 ± 0.0003 μm, with half FWHMs equal to 0.0150 ± 0.0005 μm and 0.0061 ± 0.0005 μm, respectively (red dashed line in Fig. 2d). The combination of a Gaussian and a Lorentzian component does not satisfactorily reproduce the band shape. Moreover, unlike Charon's feature, the intersection point between these two components in Europa's spectrum is depressed relative to the band continuum. The spectral feature in the Europa spectrum has been ascribed to a complex water/organic-rich molecular environment[12], given the good agreement with the laboratory spectrum of an ice mixture containing CO_2, H_2O, and CH_3OH [1:0.8:0.9] at 114 K[21] (orange dashed line in Fig. 2d). The profile of the ν_3 CO_2 absorption band is known to be strongly distorted by the presence of polar (e.g., H_2O and CH_3OH) and non-polar species (e.g., CO, O_2, and CH_4) in the surrounding ice matrix[27,28]. While we do not provide a definitive assignment to this feature, we remain open to the possibility of CO_2 embedded in a complex water/organic-rich molecular environment (referred to as complexed CO_2), akin to that of Europa[12], as an explanation for the 4.23-μm absorption band observed in the spectrum of Charon.

An alternative interpretation suggests that the observed spectral feature might not result from two separate absorption bands, but possibly from the presence of a Fresnel peak of CO_2 ice at 4.265 μm, contributing to the appearance of a double-peaked structure. This is particularly relevant when visualizing a two-layered structure where amorphous H_2O ice and crystalline CO_2 particles overlay a bed of crystalline H_2O ice and tholin-like materials (Fig. 3). Impinging radiation like solar wind can amorphize a thin rim of crystalline icy grains, especially at Charon's cold temperatures. In such a configuration, the Fresnel reflection at the interface between these two layers becomes significant and must be considered. The model shown as a red solid line in Fig. 3 consists of an areal mixture of two distinct surface units: the first comprises an intimate mixture of crystalline H_2O ice, amorphous H_2O ice, crystalline CO_2 ice, and tholin-like materials (r_{unit_1}); the second unit is characterized by a two-layer medium dominated by amorphous H_2O ice and crystalline CO_2 on top of crystalline H_2O ice and tholins (r_{unit_2}). Further elaboration on this scenario is provided in the "Spectral modeling" section in the Methods. This model displays two Fresnel peaks, one due to H_2O ice at 3.1 μm and one at 4.265 μm due to crystalline CO_2. While the match is not perfect, it is important to stress that the exact position of the CO_2 Fresnel peak strongly depends on the adopted CO_2 optical constants and their temperatures. Also, the overall model is challenged by the lack of a robust set of optical constants for tholin-like materials at long wavelengths.

https://doi.org/10.1038/s41467-024-51826-4

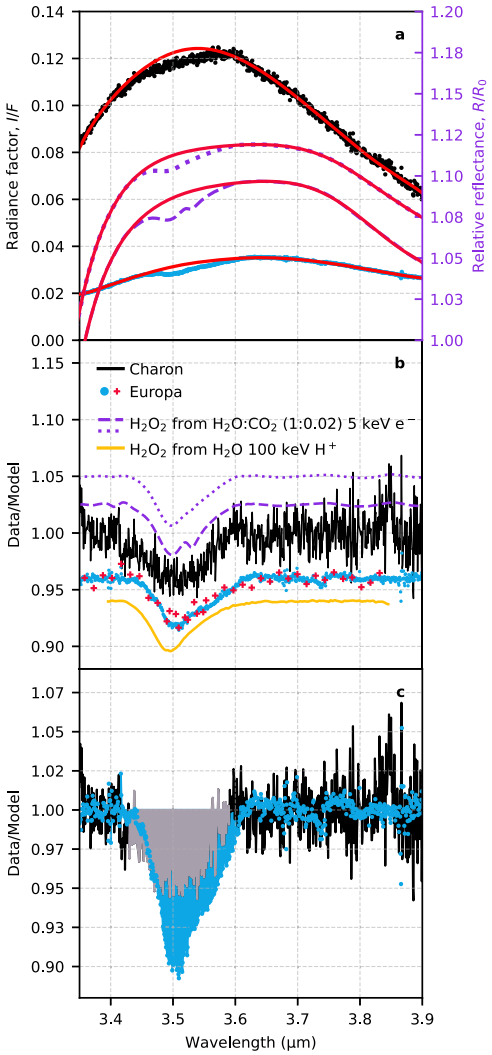

Fig. 4 | The nature of the 3.5-μm feature. a JWST observations of Charon (black points) and Europa (normalized to Charon's *I*/*F* level at 2.52–2.54 μm, cyan points) are shown alongside infrared absorption studies detailing the effects of 5 keV electron irradiation on CO_2 diluted in H_2O ice films. Two specific irradiation fluences are shown: 9.00×10^{15} e^- cm^{-2} (dotted magenta) and 9.30×10^{17} e^- cm^{-2} (dashed magenta line). The red lines show the baseline continuum fit. **b** Spectra in panel **a**, with continuum removed, are compared to the spectrum of H_2O_2 resulting from 100 keV H^+ irradiation of pure H_2O ice[30] (yellow solid line) and the spectrum of Europa from Galileo/NIMS[31] (red crosses). All spectra are normalized to Charon's band depth. **c** The continuum-removed spectra of Charon (gray) and Europa (cyan), each maintaining their native band depths. Source data are provided as a Source Data file.

Although we do not rule out the idea of complexed CO_2 or CO_2 diluted in H_2O ice and exposed to radiation, possibly in conjunction with another compound causing the short-wavelength lobe of the dual-peaked feature, our preferred interpretation for the double-peaked ν_3 band is that it originates from crystalline CO_2 and amorphous H_2O ice resting atop a layer of crystalline H_2O ice and tholins. This may be in conjunction with CO_2 that has undergone irradiation. This explanation is particularly convincing as it accounts for the characteristics of both the $\nu_1 + \nu_3$ and ν_3 bands and aligns with the geological data of Charon as reported by the New Horizons mission. Furthermore, laboratory data do not adequately match the short-wavelength lobe of the double-peaked feature, despite considering various environmental conditions.

Hydrogen peroxide detection

The JWST reflectance spectrum of Charon features a distinctive plateau around 3.50 μm (Fig. 4a). To determine whether this spectral feature can be attributed to H_2O_2, we conducted a thorough comparison with JWST observations of Europa[12] and laboratory spectra of irradiated H_2O ice films[29,30]. Notably, H_2O_2 has been conclusively identified on Europa's surface via the 3.5-μm infrared absorption band[31,32], and it is recognized as a product of radiolytic processes of H_2O ice[30,31,33]. Considering the identification of CO_2 on Charon's surface as well as on Europa, the results of our irradiation experiments with H_2O–CO_2 ice mixtures—containing a 2% CO_2 concentration comparable to that on Charon—are especially relevant for this analysis (see the "Laboratory experiments" section in the Methods for a detailed description of these experiments).

To characterize the spectral shape of the observed 3.5-μm spectral feature, we performed a non-linear baseline subtraction. Given that crystalline H_2O ice alone appears insufficient to reproduce the spectral shape of the continuum, and considering the uncertainties associated with optical constants of amorphous H_2O ice in this wavelength range[34,35], we opted for a polynomial baseline subtraction. The polynomial fit for constructing the continuum was applied across a wavelength range from 3.35 to 3.92 μm while masking the absorption region between 3.42 and 3.60 μm. This technique was consistently implemented to the entire data set under investigation, which includes the observed Charon and Europa spectra, as well as our laboratory measurements of CO_2 diluted in H_2O, before and after irradiation (Fig. 4a). We applied a polynomial fit that reproduces the spectrum of H_2O:CO_2 before irradiation, which does not display the 3.5-μm band. In this way, we ensure the adoption of a physically reasonable baseline that does not introduce extraneous structures[30].

Our experiments demonstrate that irradiation of a 1.5 μm-thick H_2O ice film containing 2% CO_2 with 5 keV electrons (e^-) leads to the formation of H_2O_2. Figure 4 presents two spectra corresponding to distinct irradiation fluences: 9.00×10^{15} e^- cm^{-2} (magenta dotted line) and 9.30×10^{17} e^- cm^{-2} (magenta dashed line). The asymmetric 3.5-μm spectral feature has an FWHM of 0.078 μm in the first case, and 0.081 μm (with an appearance of a shoulder feature at 3.53 μm) in the second. This is in line with other laboratory findings on H_2O_2 production; for instance, the yellow spectrum in Fig. 4 resulting from irradiation of pure H_2O ice by 100 keV H^+ has an FWHM of 0.079 μm[30].

The width of the 3.5-μm absorption band can be slightly influenced by the choice of continuum, such as the polynomial order or the selection of the masking zone. Additionally, the shape of the 3.5-μm band undergoes a notable alteration with varying irradiation fluence on the H_2O:CO_2 (1:0.02) mixture. As irradiation fluence increases, structures on the long-wavelength shoulder of the H_2O_2 absorption become increasingly pronounced (see comparison between magenta dashed and dotted lines in Fig. 4b). These structures are likely attributable to by-products like CH_3OH[36]. Specifically, the profile of the 3.5-μm absorption resulting from the irradiation of CO_2 diluted in H_2O can be decomposed into two distinct components: the first component, centered around 3.5 μm, is associated with H_2O_2; the second, sharper and centered at approximately 3.53 μm, is linked to other species like CH_3OH[36]. This latter feature, which becomes more pronounced with increasing irradiation fluence, subtly broadens the FWHM of the band, differentiating it from the H_2O_2 absorption observed when pure H_2O ice is irradiated.

The profile of Charon's absorption at 3.5 μm, obtained following continuum removal (black line, Fig. 4b), is in remarkable agreement with the H_2O_2 feature produced from irradiation of pure H_2O ice[30] and CO_2 diluted in H_2O. The agreement of Charon's 3.5-μm absorption (FWHM of 0.100 μm) with Europa's H_2O_2 feature detected by the Galileo Near Infrared Mapping Spectrometer (NIMS)[31] (red crosses in Fig. 4b) and JWST[12] (cyan points in Fig. 4b, FWHM = 0.092 μm) further strengthens the H_2O_2 attribution.

In the JWST spectrum of Europa, subtle structures appear on the long-wavelength shoulder of the H_2O_2 absorption, similar to those in irradiated H_2O ice films containing 2% CO_2. If these structures are confirmed by data processing with the latest JWST pipeline, they could be attributed to carbon-bearing organics. These intriguing features are less obvious in Charon's spectrum, likely due to the lower signal-to-noise ratio. We present spectra at two fluence levels to highlight the emergence of this shoulder feature around 3.53 μm. The intermediate fluence corresponds to approximately 1400 Earth-years, while the higher fluence represents about 140,000 Earth-years of radiation exposure on Charon, given 1-keV solar wind impinging at a 10^{10} m^{-2} s^{-1} flux[37]. While Galactic Cosmic Rays (GCRs) penetrate deeper into the regolith than the solar wind, accumulating a dose of 1 eV per water molecule at about 50-μm depth requires approximately 25 million years[38]. This depth of 50 μm aligns with the sensing capabilities of infrared observations in crystalline H_2O ice at temperatures around 40 K and wavelengths near 3.5 μm[34]. In contrast, the solar wind can deliver this dose at the top 50-nm veneer in only about 5 years. Micrometeoroid impacts may further facilitate the penetration of H_2O_2, initially produced by the solar wind, deeper into the surface while also exposing fresh material to the solar wind[39].

The H_2O_2 absorption on Charon is more than two times weaker than the analogous feature observed in the average spectrum of Europa's leading hemisphere (Fig. 4c). This reduced band depth implies a diminished H_2O_2 abundance on Charon relative to Europa. Further details on this comparison are discussed in the "Discussion" section.

Compositional inventory beyond carbon dioxide and hydrogen peroxide

In line with prior measurements, the JWST spectrum reveals a feature at 2.210 ± 0.001 μm. This has been ascribed to ammoniated species, as supported by earlier studies[3,4,7]. Though the existence of NH_3-bearing species on Charon was established before the JWST observations, the exact nature of these species (e.g., NH_3 frozen within the H_2O ice, superficial coatings of NH_3 ice, NH_3 combined with H_2O in one or more hydrated phases, and ammoniated salts) remained undetermined[8]. Modeling the continuum region around 2.0 μm reveals an additional band at 1.990 ± 0.001 μm. The positions and widths of these two absorption bands are most consistent with H_2O–NH_3 ice mixtures (Supplementary Fig. 1), with an NH_3 concentration of approximately 1%[40] (see the "Ammoniated species" section in the Methods for additional details).

Our analysis of Charon's 3-μm spectral region, as detailed in the "Spectral modeling" section of the Methods, reveals the presence of amorphous H_2O ice, which accounts for approximately 20% of the surface. This finding contrasts with previous studies that have primarily detected crystalline H_2O ice, constituting at least 90% of the surface composition, in the shorter wavelength range below 2.5 μm[5]. These studies suggested a minimal presence of amorphous H_2O ice, a conclusion also supported by New Horizons data analyses, which did not favor including amorphous H_2O ice in spectral models for wavelengths of 1.2–2.5 μm[8]. The disparity in H_2O ice absorption coefficients at different wavelengths provides further insight. At 40 K, the crystalline H_2O ice absorption bands at 1.5 and 2.0 μm present peak absorption coefficients of approximately 50 and 100 cm^{-1}, respectively[41]. These values correspond to photon penetration depths in ice of around 200 and 100 μm, respectively. In contrast, the average penetration depth associated with the 3.0-μm H_2O ice absorption band (2.8–3.3 μm) is less than 5 μm. As a result, spectroscopic measurements in this wavelength range investigate a surface layer less than a few microns in depth. The necessity to include amorphous H_2O ice for accurately modeling the 3-μm region, coupled with the absence of amorphous ice signatures in spectroscopic measurements below 2.5 μm, leads us to conclude that amorphous H_2O ice is present primarily in a very thin surface layer.

In summary, the Charon spectra reveal the presence of H_2O ice in both crystalline and amorphous phases, along with CO_2, H_2O_2, and NH_3 diluted in H_2O. There is no clear evidence of any additional compounds (e.g., CH_4, CO, and CH_3OH). An absorption band centered around 1.8 μm is seen in the JWST spectrum and was also observed in New Horizons spectra but possibly attributed to flat-field artifacts. The nature of this feature remains uncertain at this point.

Discussion

We explore multiple potential sources for the solid CO_2 detected on Charon, which includes endogenic, exogenic, and in-situ formation from radiation processing. Each source is considered for its ability to contribute to the spectral features observed on Charon, with careful consideration of the moon's environmental conditions. This discussion aims to decipher the complex processes that could have contributed to shaping Charon's present composition, as indicated by spectroscopic evidence.

Exogenous impactors could have delivered CO_2 to Charon's surface and/or exposed subsurface endogenic CO_2 reservoirs through cratering events. In such an instance, CO_2 absorption is presumably enhanced in the bright ejecta blankets of geologically young craters, similar to the ammoniated species[2,6,8], due to the exposure of fresh material. The sharp 2.7-μm Lorentzian absorption indicates that some fraction of the surficial CO_2 has segregated from the surrounding H_2O ice matrix and crystallized, possibly due to thermal heating from both the summer northern hemisphere and the heat generated during the cratering process. In this scenario, the long-wavelength absorption band around 4.23 μm could result from a stratification scattering effect within the ice, possibly in conjunction with irradiation products of the endogenic/exogenic CO_2 that has not segregated. Supporting the notion of endogenic CO_2, analyses of cometary nuclei through their comae observed at heliocentric distances less than 2.5 au have demonstrated that the CO_2/H_2O ratio ranges between a few percent and 30%[42,43]. This aligns with our estimate of the CO_2 amount responsible for the 2.7-μm absorption being on the order of 2%. Additionally, the presence of NH_3 diluted in H_2O at the 1% level aligns with cometary measurements[40], reinforcing the idea of heritage compounds being exposed. If Charon (and Pluto) accreted from planetesimals containing cometary fractions of CO_2, there could have originally been a significant amount of it in their interiors. However, the fate of the endogenous CO_2 during the Charon-forming impact event remains uncertain, leading us to consider the role of in-situ formation of CO_2 from radiation processing.

Processing of Charon's hydrocarbons by interplanetary medium (IPM) and solar Lyman α (Ly-α) UV photons, solar wind ions and electrons, and GCRs could yield a fraction of the observed CO_2. Charon's winter hemisphere serves as a cold trap for CH_4 escaping Pluto[9]. The photolytic breakdown of condensed CH_4 by Ly-α photons results in the formation of higher-order hydrocarbons[9,10]. These Ly-α photons could also dissociate H_2O molecules in the vicinity of CH_4 to induce reactions that synthesize CO_2[44,45] and other CHO species, such as CH_3OH and carbonic acid. Spring sunrise on the winter hemisphere prompts rapid sublimation of unphotolyzed CH_4, but heavier hydrocarbons, including ethane, persist on Charon's warming surface (60 K maximum summer temperature) and undergo further processing by the solar wind. Radiolysis of hydrocarbons intimately mixed with H_2O ice by the solar wind keV H^+ and alpha particles could contribute to Charon's CO_2 inventory[46]. Additionally, carbon ions in the solar wind can be implanted into Charon's icy regolith and react with H_2O molecules to synthesize CO_2[47]. However, this mechanism is comparatively less efficient due to its low yield (0.4 CO_2 per carbon ion) and a significantly reduced carbon ion flux, which is four orders of magnitude lower than

that of H^+. Moreover, energetic GCRs further process Charon's hydrocarbon-rich H_2O ice, generating CO_2 at greater depths compared to the solar wind and Ly-α photons. The band profile of the ν_3 CO_2 absorption band generated from photolysis/radiolysis of hydrocarbon–H_2O ice mixtures in multiple laboratory experiments reasonably matches Charon's 4.27-μm Lorentzian peak[46].

Radiolysis at the interfaces between carbon and H_2O, involving carbonaceous residues embedded in H_2O ice, offers an additional mechanism for producing solid CO_2 on Charon's surface[48–50]. These residues could be native to Charon or derived exogenously from Kuiper belt impactors or interplanetary dust particles[8]. The radiolytic yield for each interface is modest, around 0.05–0.1 CO_2 molecules for every incoming proton, and the utmost quantity produced does not surpass approximately a few 10^{15} CO_2 molecules cm^{-2} per interface (due to CO_2 shielding the carbon from H_2O and the destruction of CO_2 by incident ions)[50]. However, the cumulative effects of multiple interfaces within Charon's meters-thick radiolytic layer (considering GCRs) make this a viable mechanism that adds to Charon's CO_2 stockpile. The 4.27-μm CO_2 absorption band observed on the surface of Charon could be produced by this mechanism after diffusion or desorption followed by gravitational return[50]. The interfacial oxidation reaction likely prevents complete carbonization of the dark neutral absorber or tholins thought to be present at levels of up to 50% by volume fraction[3,8]. These dark absorbers likely contribute to the greyish coloration on Charon, especially toward lower latitudes below ~70°.

In summary, CO_2 produced in situ from radiation processing could contribute to the most surficial (approximately 1-μm penetration depth) CO_2 layer. However, laboratory experiments simulating these formation mechanisms do not show the resulting 2.7-μm absorption band, challenging the possibility of assessing whether these processes alone would be compatible with the overall CO_2 spectral behavior observed on Charon. Given the laboratory results for CO_2 embedded in other compounds before and after irradiation, we speculate that the 2.7-μm feature resulting from in-situ processing might not be consistent with the observations, and thermal annealing would possibly be required. Further discrimination between these processes has potentially interesting implications for the fate of CO_2 Charon may have inherited from the proto-Pluto and the Charon-forming impactor during and after the formation of Charon itself.

The detection of H_2O_2 is a clear demonstration of the influence of radiolysis and photolysis on Charon's surface. The creation of H_2O_2 through radiolytic and photolytic processing of H_2O ice has been thoroughly studied and is a fairly established process on small bodies throughout the Solar System[30,33,51–55]. Laboratory measurements have been instrumental in explaining the detection and concentration of H_2O_2 on Europa[30,31,33]. H_2O_2 formation occurs from the combination of neighboring OH radicals, which originate from the breakup of H_2O molecules due to incoming ions, electrons, or photons.

Charon's global H_2O ice-rich surface is continuously processed by GCRs, IPM Ly-α photons[56], as well as by solar wind ions and electrons, and solar UV photons on the sunlit hemisphere[37,57], collectively synthesizing H_2O_2. Despite their low fluxes, cosmic rays penetrate deeper into Charon's icy regolith, depositing energy to induce radiolysis meters below the surface. In comparison, solar wind and Ly-α photons only process the topmost 50-nm veneer, approximately. Micrometeroid gardening can lead to upward mixing of GCR-generated H_2O_2 to depths accessible to remote sensing (about 0.1–100 μm)[39,58].

Contrary to radiolysis of pure H_2O ice, radiolysis of H_2O–CO_2 ice mixtures not only produces H_2O_2 but also yields formaldehyde, carbonic acid, and CH_3OH[59–61]. At high irradiation fluence (10^{18} e^- cm^{-2}, equivalent to approximately 10^5 years of solar wind radiation exposure at Charon[62]), a shoulder, indicative of CH_3OH, becomes evident at 3.53 μm in the laboratory spectrum, piercing through the nominal asymmetric H_2O_2 absorption. While this CH_3OH-related shoulder at 3.53 μm is not observable in the Charon JWST/NIRSpec spectra, the presence of CO_2 implies that the 3.5-μm absorption feature might not be solely attributable to H_2O_2. Consequently, we cannot dismiss the potential enhancing contribution of overlapping absorptions from other radiolytic organics. Additionally, weaker CH_3OH absorption bands, expected around 2.27 μm, remain undetected as well.

The radiolytic synthesis of H_2O_2 is also consistent with the presence of amorphous H_2O ice on Charon's surface. Impinging radiation, as well as flash sublimation from impact heating followed by condensation on a cold surface, can break down the crystalline structure[63]. The amorphized ice retains its disordered structure more effectively at Charon's colder temperatures.

We find that the abundance of H_2O_2 on Charon is approximately a factor of two lower compared to Europa. Charon's surface temperature is cooler than Europa's (approximately 50 K[22] versus 90–130 K[64]). While laboratory studies suggest an increased production of H_2O_2 at lower temperatures[30], the differences between Europa and Charon H_2O_2 content could be attributed to different radiation environments encountered by the two satellites. Europa experiences intense bombardment from charged particles (H^+, S^{n+}, O^{n+}) trapped in the Jovian magnetosphere, with energies ranging from tens of keV to MeV[65]. These levels significantly exceed the keV solar wind impinging on Charon[37]. Additionally, solid NH_3, present on Charon's surface, can also react with and destroy H_2O_2 at temperatures exceeding 50 K[66], which may partially explain the lower H_2O_2 levels on Charon compared to Europa. Furthermore, different concentrations of CO_2 may also affect the abundance of radiolytic H_2O_2. Systematic laboratory work investigating the impact of irradiation on H_2O–CO_2 mixtures, with diverse dilution levels at various temperatures, is essential to further explore the similarities and differences between these two intriguing satellites.

To conclude, the inaugural observations of Charon by JWST have significantly advanced our comprehension of its surface composition, revealing a stratified surface rich in crystalline H_2O ice with NH_3 diluted in H_2O ice at penetration depths of approximately 100 μm. Additionally, a layer of pure crystalline CO_2 is evident at shallower penetration depths of about 5 μm. This feature is likely attributable to an endogenous source, unearthed by external impacts. This layering configuration is believed to cause a scattering effect, which may account for the peculiarly strong CO_2 absorption band at longer wavelengths. Moreover, the surface is undergoing continuous alteration by photolysis and radiolysis, which contribute to the CO_2 inventory and are responsible for the presence of H_2O_2 and amorphous H_2O ice.

Methods

Data reduction

The raw uncalibrated data (Supplementary Table 1) were processed with Version 1.11.1 of the official JWST pipeline[67]. Relevant calibration reference files were automatically acquired from build `jwst_1097.pmap` of the JWST Calibration Reference Data System (CRDS). The stacks of non-destructive reads were first converted to count rate (slope) images by applying Stage 1 of the JWST pipeline. This step was followed by the manual removal of residual correlated detector readnoise (so-called 1/*f* noise) using a 200-pixel-wide moving median filter on the off-sky pixels within each detector column. Next, Stage 2 of the JWST pipeline was applied to the readnoise-corrected count rate images, resulting in wavelength-calibrated, flux-calibrated, and spatially-rectified spectral cubes for each grating, detector, and dither (i.e., two dithered exposures were acquired in each instrument setting, resulting in six IFU cubes per observation, see Supplementary Table 1). We ran the JWST pipeline locally, using the default settings for both stages. Each IFU cube consists of a stack of over 1000 3.0″ × 3.0″ sky-projected images, one for each wavelength. The following data reduction steps include: (1) extracting Charon's spectrum, (2) correcting for flux contamination due to Pluto, (3) adjusting for flux losses outside the extraction aperture, and (4) converting Charon's flux to *I*/*F*.

Step 1: Spectral extraction. Spectral extraction was carried out using a specialized empirical point-spread function (PSF) fitting methodology. We calculated the centroid of Charon using a 2D Gaussian fit (after masking Pluto) and placed a 5 × 5 pixel extraction aperture centered on the centroid position, rounded to the nearest integer pixel. For a given image k in the IFU cube, we constructed a local template PSF by calculating the 2D median of all images within the range ($k-10$, $k+10$). After setting all pixel values outside of the 5 × 5 extraction aperture to zero and normalizing to an integrated flux of unity, we used an error-weighted least-squares minimization routine to fit this template PSF to the image k, with a multiplicative scaling factor as a free parameter. Fitting was done twice, the second time after masking 7-σ outliers from the residuals of the first fit. This process was done on every image within each IFU cube, with the corresponding best-fit scaling factor defining the extracted spectra at every grating/detector/dither setting. The spectrum resulting from this approach was compared with the one obtained through straightforward circular or square aperture extraction techniques. While both methods produce notably consistent outcomes, the PSF technique yields a significantly enhanced signal-to-noise ratio.

Step 2: Correcting for Pluto's flux contamination. Upon examining the IFU images (Fig. 1, panel e), it is evident that while Pluto and Charon are spatially separated, there is minor blending of the fluxes from the two binary components, with Charon positioned on a diffraction spike of Pluto's PSF. To mitigate Pluto's contamination in Charon's extracted flux, we placed a box centered along the line joining Pluto and Charon, lying precisely opposite to Charon relative to Pluto. This "anti-Charon" box had the same size as the one used for source extraction, i.e., 5 × 5 pixels. We summed the flux within the anti-Charon box to obtain an estimate of Pluto's contamination at Charon. To improve the quality of the contamination spectrum, we extracted the high signal-to-noise spectrum of Pluto using the same PSF fitting technique outlined above and smoothly scaled it to match the flux level measured within the contamination box at every wavelength. The resultant scaled spectrum of Pluto was then subtracted from Charon's spectrum to remove Pluto's flux contamination (Supplementary Fig. 4).

Step 3: Correction for flux losses. The close proximity of the two binary components necessitated a relatively small extraction aperture for Charon, which left a wavelength-dependent fraction of Charon's PSF outside of the aperture. To correct for flux losses and retrieve the full unbiased flux of Charon, we utilized NIRSpec observations of the G2V-type solar standard star GSPC P330-E, obtained as part of the flux calibration program #1538. By extracting the star's spectrum using an identical extraction methodology and aperture size as those used for our spectral extraction of Charon, and then dividing it by the calibrated CALSPEC spectrum of the star[68], we obtained a ratio spectrum that quantifies the fractional amount of a point source's total flux that lies within a 5 × 5 pixel aperture. We fitted cubic polynomial curves to the ratio spectra in each of the grating/detector combinations and divided these curves from the decontaminated Charon spectra to obtain the flux-corrected spectra. We then combined each pair of dithered spectra using weighted mean averaging. Lastly, we applied a 30-point-wide 3-σ moving median filter on each spectrum to arrive at the final spectrum of Charon, which has units of MJy/sr.

Step 4: Conversion to I/F. The spectra resulting from Step 3 were then converted to $I/F = \pi I r^2/F_\odot$, where I is the radiance at the detector defined as power per unit area per unit solid angle, r is the target's heliocentric distance in astronomical units and $F_\odot$ is the solar flux at 1 au. The radius used to determine the area of Charon in pixel units is 606 km[69]. The solar flux at 1 au was generated using the planetary spectrum generator (PSG)[70,71], which accounts for the Doppler shift associated with the orbital parameters of both Charon and JWST at the time of the observations, as well as the spectral resolution of the NIRSpec filters. PSG adopts a composite spectrum of the Sun, combining the solar spectrum modeled by Kurucz in the wavelength range 0.4–2.0 μm (see http://kurucz.harvard.edu) and the spectrum measured by the Atmospheric Chemistry Experiment Fourier Transform Spectrometer (ACE-FTS) instrument onboard SCISAT-1 in the range 2–14 μm[72]. The comparison of this composite spectrum with the Kurucz model of the Sun, sourced from the CALSPEC database[68], both at a resolving power of 5000, is shown in Supplementary Fig. 5. The Kurucz model does not adequately reproduce the observations beyond approximately 4.3 μm. Consequently, we opted for the composite solar spectrum provided by PSG for our analyses.

Laboratory experiments

To facilitate the interpretation of Charon's surficial CO_2 and H_2O_2, we carried out a series of irradiation experiments on H_2O–CO_2 ice mixtures. We deposited H_2O ice films (approximately 1.5 μm thick) containing trace amounts of CO_2 (about 2%, which is similar to the CO_2 abundance estimated on Charon based on spectral modeling of the 2.7-μm $\nu_1+\nu_3$ CO_2 combination band; see text for details) relative to H_2O ice onto a gold-coated quartz crystal microbalance (QCM). The QCM substrate was cooled to 70 K prior to film deposition, slightly higher than the 60 K maximum surface temperature predicted for Charon's sunlight hemisphere[9]. An intimate H_2O–CO_2 mixture of precise composition was obtained by simultaneously condensing H_2O vapor and CO_2 gas onto the QCM from two separate doses. We began the deposition process by introducing CO_2 gas to establish a baseline condensation rate on the QCM, typically around 0.5–0.7 nm min^{-1}. Subsequently, we leaked H_2O into the system, increasing the deposition rate to approximately 25–35 nm min^{-1}. As the ice thickness neared the target of 1.5 μm on the QCM, we closed the H_2O doser first in order to ensure that the terminal CO_2 deposition rate remained within 10% of the initial rate observed at the start of deposition. This technique of simultaneous deposition allows for precise calculation of the relative CO_2 abundance in our mixtures[73]. A specular reflectance infrared spectrum of the ice mixture, denoted by R, was collected over the wavelength range between 1 and 16 μm at 2 cm^{-1} resolution using a Thermo-Nicolet iS50 FTIR spectrometer. The resulting spectra are expressed as relative reflectance R/R_o or in optical depth units, $-\ln(R/R_o)$, where R_o is the reflectance of the bare gold substrate. We note that the spectra of laboratory ice films, obtained in specular reflectance, differ from the directional hemispherical reflectance spectra of Charon's granular icy regolith. This discrepancy is primarily due to the absence of anisotropic scatterers and surface roughness in our laboratory ice films. Despite these differences, comparing the absorption band profiles—such as peak centers, asymmetry, and widths—between our laboratory data and astronomical observations proves to be a powerful method for deciphering the state or phases of surface constituents like CO_2 and H_2O_2 on Charon, as demonstrated in our study.

The H_2O–CO_2 films were subject to irradiation from 5 keV electrons produced by a Kimball Physics EGG-3101 Electron Source. Additional spectra were acquired following incremental fluence/dose steps to track compositional changes in the ice film from irradiation. The key results pertaining to the effects of radiation on the 2.7- and 4.24-μm CO_2 absorption bands and the 3.5-μm H_2O_2 feature are discussed in the main text. These experiments were conducted in an ultra-high vacuum chamber with a base pressure of about 10^{-10} Torr.

Spectral modeling

To model the 2.0-μm region (Supplementary Fig. 1a), we employed the Hapke radiative transfer theory[14] and considered an intimate mixture of crystalline H_2O ice at temperatures of 50 and 70 K[41] and a tholin-like material synthesized from an initial gas composition of N_2:CH_4 = 99%:1% with 500 ppm of CO[74]. This approach aligns with methodologies utilized in previous spectral modeling of Charon's spectra in the near-IR wavelength range up to 2.5 μm[3,8]. The fit to the JWST observations was carried out within the wavelength range

1.8–2.3 μm. The fit was weighted such that the wavelength range between 2.18 μm and 2.28 μm, where ammoniated species present a strong absorption band, did not affect the modeling results. The plausible identity of the ammoniated species was probed through the relative residuals (data/model) in the 2.2-μm spectral range (see Methods section "Ammoniated species" and Supplementary Fig. 1b). The free parameters in the model were the effective grain diameter (D_i) and the fractional volume (V_i) of each mixture component. These parameters were iteratively refined using the Levenberg–Marquardt χ^2 minimization algorithm to achieve the best fit to the observations[75]. We employed Hapke parameters obtained for Charon from a disk-integrated analysis of Hubble data at 0.55 μm and data from New Horizons' LOng-Range Reconnaissance Imager (LORRI)[15]. Specifically, our model utilized a single-lobe Henyey–Greenstein phase function[76], with the asymmetry parameter, ξ, set to −0.14. The shadow-hiding opposition effect featured an amplitude, B_0, of 0.74 and a width, h, of 0.0015. We also incorporated the effects of macroscopic roughness, setting the mean roughness slope θ to 24°. The best-fit values for the volume fraction and particle diameter are as follows: 18% and 145 μm for crystalline H_2O ice at 70 K, 65% and 35 μm for crystalline H_2O ice at 50 K, and 17% and 45 μm for tholin-like materials. We stress that the estimates of the concentration and particle size of each surface compound depend strongly on the choice of the optical properties of the darkening material (i.e., tholin-like material).

The same strategy described above was adopted to model the continuum in the wavelength range between 2.6 and 2.8 μm in order to isolate the 2.7-μm CO_2 band. To facilitate the modeling of the saturated H_2O ice absorption in the 3-μm region, an isotropic phase function with $\xi = 0$ was employed. The need for distinct photometric properties to model the data at short wavelengths (below 2.5 μm) and longer near-IR wavelengths (beyond 2.5 μm) may be attributed to these wavelength ranges probing varying penetration depths with different microscopic properties. The spectral slope between 2.6 and 2.8 μm serves as a good metric for distinguishing amorphous from crystalline H_2O ice, given that the former has a shallower slope than the latter. Adopting crystalline H_2O ice only failed to replicate the data. The best-fit model was obtained as an intimate mixture of approximately 80 μm-diameter grains, with the fractional volume (V_i) of crystalline H_2O ice at 70 K being on the order of 90% and that of amorphous H_2O ice at 60 K being about 10%. We also tested an areal mixture of crystalline H_2O ice at 70 K and amorphous H_2O ice at 60 K, achieving a statistically equivalent best fit with approximately 80 μm-diameter grains. In this mixture, the fractional area (F_i) covered by crystalline H_2O ice is 85%, while that covered by amorphous H_2O ice is 15%. This model is illustrated in Fig. 2a (red solid line).

For the wavelength range between 2.66 and 2.8 μm, including the CO_2 band, we required an areal mixture of two components: crystalline H_2O ice at 70 K and aggregates of amorphous H_2O ice at 60 K with crystalline CO_2[16]. For the aggregates, we estimated the real and imaginary parts of the refractive index as a function of wavelength, λ, using effective medium theory (specifically, the Bruggeman mixing formula[77]). This technique preserves the spectral properties of each component within the aggregate and assumes that the medium's end-members are distinct from one another at the molecular level. The free parameters in this case were the areal fraction and particle diameter of each component, and the percentage of crystalline CO_2 relative to amorphous H_2O ice. Including crystalline CO_2 ice in amorphous H_2O ice helped to attenuate the 2.78-μm absorption band compared to the 2.7-μm band. The best-fit model consisted of an areal mixture of 80% crystalline H_2O ice (with approximately 115-μm particle diameter) and 20% amorphous H_2O ice with 12% inclusions of crystalline CO_2 (with approximately 7-μm particle diameter). This corresponds to 2% crystalline CO_2 and 18% amorphous H_2O ice. The comparison between the data and the best-fit model is shown in Supplementary Fig. 3.

We developed a model that simultaneously fits the wavelength ranges 2.5–3.2 and 4.1–4.5 μm to model the CO_2 $\nu_1 + \nu_3$ combination band near 2.70 μm and the asymmetric stretching fundamental ν_3 at 4.27 μm. Analysis of spatially resolved data from New Horizons highlights a surface primarily composed of crystalline H_2O ice and refractory materials, contributing to the gray coloration at visible wavelengths, with the north polar cap being an exception. An enhanced abundance of H_2O ice and ammoniated species is noted in the bright ejecta blankets of geologically young craters. In light of these findings, and to incorporate the new detections of crystalline CO_2 and amorphous H_2O ice on Charon's surface, we formulated a compositional model to replicate these observed surface characteristics. This model consists of an areal mixture of two distinct surface units: the first comprises an intimate mixture of crystalline H_2O ice, amorphous H_2O ice, crystalline CO_2 ice, and tholin-like materials (r_{unit_1}); the second unit is characterized by a two-layer medium dominated by amorphous H_2O ice and crystalline CO_2 on top of crystalline H_2O ice and tholins (r_{unit_2}). This model serves as a qualitative attempt to emulate the observed spectral features at long wavelengths, taking into account the known geology of Charon (see Fig. 3). In our model, we considered the Fresnel reflection occurring at the interface between the layered media. This reflection is attenuated by the extinction resulting from the particles present in the top layer. The optical constants of the top and bottom layers ($n(\lambda)$, $k(\lambda)$) were estimated using the effective medium theory (specifically, the Bruggeman mixing formula[77]).

We encountered challenges in developing a Hapke model similar to those described above to accurately reproduce the continuum near the 3.5-μm band of H_2O_2. The optical constants of amorphous H_2O ice in this region exhibit uncertainty[34], and the continuum cannot be faithfully reproduced using only the optical constants of crystalline H_2O ice. Consequently, we resorted to employing a polynomial fit to define the continuum for this band, as described in the main body of the paper.

Ammoniated species

To investigate the nature of the 2.21-μm absorption band on Charon, we modeled the 2.0-μm region without including a contribution from NH_3-bearing compounds and instead de-weighted the data in the 2.18–2.28 μm range, where these materials typically have an absorption band. This is purposely done because the available optical constants for these hydrates and salts are limited and cannot account for all the possible chemical variants of these species[40,78–80]. The spectral region around 2.0 μm is well represented by an intimate mixture of crystalline H_2O ice and tholin-like material, as shown by the red line in Supplementary Fig. 1a (refer to the "Spectral modeling" section in the Methods for comprehensive details on the modeling analysis). The resultant relative residual spectrum (data/model) showcases a feature with a center at 2.210 ± 0.001 μm (calculated from a Gaussian fit). Another feature occurs at 1.990 ± 0.001, which overlaps with the much stronger H_2O ice band. The position and width of these absorption bands are most consistent with H_2O–NH_3 ice mixtures (see Supplementary Fig. 1b). According to laboratory data, the central wavelengths of the 2.0- and 2.2-μm NH_3 bands vary depending on the NH_3-to-H_2O ratio. The 2.0-μm NH_3 band shifts from 2.006 ± 0.003 μm to 1.993 ± 0.003 μm as the percentage of NH_3 decreases from 100% to 1%[40]. The 2.2-μm NH_3 band center shifts from 2.229 ± 0.003 μm to 2.208 ± 0.003 μm over the same range[40]. Consequently, the detected positions of the NH_3 bands in the JWST data align with an NH_3 concentration of approximately 1%.

Data availability

The JWST data used in this study (see Supplementary Table 1 for details on the JWST observations) are publicly available from the Space Telescope Science Institute's Mikulski Archive for Space Telescopes

(https://mast.stsci.edu/). The grand-average spectrum of Charon and the infrared absorption spectra detailing the effects of 5 keV electron irradiation on CO_2 diluted in H_2O ice films generated in this study have been deposited in the Zenodo database. The high-quality global mosaic of Charon, compiled from nearly all the New Horizons/LORRI and MVIC highest-resolution images and used to produce panels a through d in Fig. 1, was obtained from the USGS Astrogeology Science Center website as an ISIS3 cube file (https://astrogeology.usgs.gov/search/map/new-horizon-global-mosaics). The New Horizons/LEISA scan of Charon used to generate the spectra and maps shown in Fig. 1g and Supplementary Fig. 1 (scan name C_LEISA_HIRES scan, Mission Elapsed Time 0299175509) is available at the PDS Small Bodies Node (https://pdssbn.astro.umd.edu/holdings/nh-p_psa-leisa_mvic-5-comp-v1.0/data/spec/). The datasets generated as part of this study are available from the corresponding author on request. Source data are provided in this paper.

Code availability

The JWST science data calibration pipeline is at https://github.com/spacetelescope/jwst; the Planetary Spectrum Generator is at https://psg.gsfc.nasa.gov/. The spectral modeling code used in this study is part of a multifaceted toolset that employs Hapke, Mie, and effective medium theories to analyze planetary surfaces and cometary comae and cannot be provided independently. Details on the numerical simulations and the spectral modeling tool are discussed within the text and are available from the corresponding author upon request. The MCMC simulation was carried out using the publicly available `emcee` Python library (https://github.com/dfm/emcee).

References

1. Stern, S. A. et al. The Pluto system: initial results from its exploration by New Horizons. *Science* **350**, aad1815 (2015).
2. Grundy, W. M. et al. Surface compositions across Pluto and Charon. *Science* **351**, aad9189 (2016).
3. Buie, M. W. & Grundy, W. M. The distribution and physical state of H_2O on Charon. *Icarus* **148**, 324–339 (2000).
4. Brown, M. E. & Calvin, W. M. Evidence for crystalline water and ammonia ices on Pluto's satellite Charon. *Science* **287**, 107–109 (2000).
5. Merlin, F. et al. Chemical and physical properties of the variegated Pluto and Charon surfaces. *Icarus* **210**, 930–943 (2010).
6. Dalle Ore, C. M. et al. Ices on Charon: distribution of H_2O and NH_3 from New Horizons LEISA observations. *Icarus* **300**, 21–32 (2018).
7. Cook, J. C. et al. Analysis of Charon's spectrum at 2.21 μm from New Horizons/LEISA and Earth-based observations. *Icarus* **389**, 115242 (2023).
8. Protopapa, S. et al. Surface composition of Charon. In *The Pluto System After New Horizons* (eds Stern, S. A., Moore, J. M., Grundy, W. M., Young, L. A. & Binzel, R. P.) 433–456 (University of Arizona Press, 2021).
9. Grundy, W. M. et al. The formation of Charon's red poles from seasonally cold-trapped volatiles. *Nature* **539**, 65–68 (2016).
10. Raut, U. et al. Charon's refractory factory. *Sci. Adv.* **8**, eabq5701 (2022).
11. Böker, T. et al. In-orbit performance of the Near-Infrared Spectrograph NIRSpec on the James Webb Space Telescope. *Publ. Astron. Soc. Pac.* **135**, 038001 (2023).
12. Villanueva, G. L. et al. Endogenous CO_2 ice mixture on the surface of Europa and no detection of plume activity. *Science* **381**, 1305–1308 (2023).
13. Trumbo, S. K. & Brown, M. E. The distribution of CO_2 on Europa indicates an internal source of carbon. *Science* **381**, 1308–1311 (2023).
14. Hapke, B. *Theory of Reflectance and Emittance Spectroscopy* (Cambridge University Press, 2012).
15. Howett, C. J. A. et al. Charon: colors and photometric properties. In *The Pluto System After New Horizons* (eds Stern, S. A., Moore, J. M., Grundy, W. M., Young, L. A. & Binzel, R. P.) 413–432 (University of Arizona Press, 2021).
16. Gerakines, P. A. & Hudson, R. L. A modified algorithm and open-source computational package for the determination of infrared optical constants relevant to astrophysics. *Astrophys. J.* **901**, 52 (2020).
17. Gerakines, P. A. & Hudson, R. L. First infrared band strengths for amorphous CO_2, an overlooked component of interstellar ices. *Astrophys. J. Lett.* **808**, L40 (2015).
18. He, J., Emtiaz, S., Boogert, A. & Vidali, G. The $^{12}CO_2$ and $^{13}CO_2$ absorption bands as tracers of the thermal history of interstellar icy grain mantles. *Astrophys. J.* **869**, 41 (2018).
19. Raut, U. & Baragiola, R. A. Sputtering and molecular synthesis induced by 100 keV protons in condensed CO_2 and relevance to the outer solar system. *Astrophys. J.* **772**, 53 (2013).
20. Bernstein, M. P., Cruikshank, D. P. & Sandford, S. A. Near-infrared laboratory spectra of solid H_2O/CO_2 and CH_3OH/CO_2 ice mixtures. *Icarus* **179**, 527–534 (2005).
21. Ehrenfreund, P. et al. Laboratory studies of thermally processed H_2O-CH_3OH-CO_2 ice mixtures and their astrophysical implications. *Astron. Astrophys.* **350**, 240–253 (1999).
22. Holler, B. J. et al. Measuring temperature and ammonia hydrate ice on Charon in 2015 from Keck/OSIRIS spectra. *Icarus* **284**, 394–406 (2017).
23. Quirico, E. & Schmitt, B. Near-infrared spectroscopy of simple hydrocarbons and carbon oxides diluted in solid N_2 and as pure ices: implications for Triton and Pluto. *Icarus* **127**, 354–378 (1997).
24. Cartwright, R. J., Emery, J. P., Rivkin, A. S., Trilling, D. E. & Pinilla-Alonso, N. Distribution of CO_2 ice on the large moons of Uranus and evidence for compositional stratification of their near-surfaces. *Icarus* **257**, 428–456 (2015).
25. Grundy, W. M. et al. Near-infrared spectral monitoring of Triton with IRTF/SpeX II: spatial distribution and evolution of ices. *Icarus* **205**, 594–604 (2010).
26. Isokoski, K., Poteet, C. A. & Linnartz, H. Highly resolved infrared spectra of pure CO_2 ice (15-75 K). *Astron. Astrophys.* **555**, A85 (2013).
27. Sandford, S. A. & Allamandola, L. J. The physical and infrared spectral properties of CO_2 in astrophysical ice analogs. *Astrophys. J.* **355**, 357 (1990).
28. Ehrenfreund, P., Boogert, A. C. A., Gerakines, P. A., Tielens, A. G. G. M. & van Dishoeck, E. F. Infrared spectroscopy of interstellar apolar ice analogs. *Astron. Astrophys.* **328**, 649–669 (1997).
29. Loeffler, M. J. & Baragiola, R. A. The state of hydrogen peroxide on Europa. *Geophys. Res. Lett.* **32**, L17202 (2005).
30. Loeffler, M. J., Raut, U., Vidal, R. A., Baragiola, R. A. & Carlson, R. W. Synthesis of hydrogen peroxide in water ice by ion irradiation. *Icarus* **180**, 265–273 (2006).
31. Carlson, R. W. et al. Hydrogen peroxide on the surface of Europa. *Science* **283**, 2062 (1999).
32. Trumbo, S. K., Brown, M. E. & Hand, K. P. H_2O_2 within chaos terrain on Europa's leading hemisphere. *Astron. J.* **158**, 127 (2019).
33. Hand, K. P. & Carlson, R. W. H_2O_2 production by high-energy electrons on icy satellites as a function of surface temperature and electron flux. *Icarus* **215**, 226–233 (2011).
34. Mastrapa, R. M., Sandford, S. A., Roush, T. L., Cruikshank, D. P. & Dalle Ore, C. M. Optical constants of amorphous and crystalline H_2O-ice: 2.5-22 μm (4000-455 cm^{-1}) optical constants of H_2O-ice. *Astrophys. J.* **701**, 1347–1356 (2009).
35. Clark, R. N. et al. The surface composition of Iapetus: mapping results from Cassini VIMS. *Icarus* **218**, 831–860 (2012).
36. Luna, R. et al. Densities, infrared band strengths, and optical constants of solid methanol. *Astron. Astrophys.* **617**, A116 (2018).

37. Bagenal, F. et al. Solar wind interaction with the Pluto system. In *The Pluto System After New Horizons* (eds Stern, S. A., Moore, J. M., Grundy, W. M., Young, L. A. & Binzel, R. P.) 379–392 (University of Arizona Press, 2021).
38. Loeffler, M. J., Tribbett, P. D., Cooper, J. F. & Sturner, S. J. A possible explanation for the presence of crystalline H_2O-ice on Kuiper Belt Objects. *Icarus* **351**, 113943 (2020).
39. Costello, E. S., Phillips, C. B., Lucey, P. G. & Ghent, R. R. Impact gardening on Europa and repercussions for possible biosignatures. *Nat. Astron.* **5**, 951–956 (2021).
40. Zheng, W., Jewitt, D. & Kaiser, R. I. Infrared spectra of ammonia-water ices. *Astrophys. J. Suppl. Ser.* **181**, 53–61 (2009).
41. Mastrapa, R. M. et al. Optical constants of amorphous and crystalline H_2O-ice in the near infrared from 1.1 to 2.6 μm. *Icarus* **197**, 307–320 (2008).
42. A'Hearn, M. F. et al. Cometary volatiles and the origin of comets. *Astrophys. J.* **758**, 29 (2012).
43. Harrington Pinto, O., Womack, M., Fernandez, Y. & Bauer, J. A Survey of CO, CO_2, and H_2O in Comets and Centaurs. *Planet. Sci. J.* **3**, 247 (2022).
44. Hodyss, R. et al. Methanol on Enceladus. *Geophys. Res. Lett.* **36**, L17103 (2009).
45. Krim, L. & Jonusas, M. VUV photolysis of CH_4-H_2O mixture in methane-rich ices: formation of large complex organic molecules in astronomical environments. *Low. Temp. Phys.* **45**, 606–614 (2019).
46. Hand, K. P. & Carlson, R. W. Laboratory spectroscopic analyses of electron irradiated alkanes and alkenes in solar system ices. *J. Geophys. Res.* **117**, E03008 (2012).
47. Strazzulla, G., Leto, G., Gomis, O. & Satorre, M. A. Implantation of carbon and nitrogen ions in water ice. *Icarus* **164**, 163–169 (2003).
48. Strazzulla, G. & Moroz, L. Ion irradiation of asphaltite as an analogue of solid hydrocarbons in the interstellar medium. *Astron. Astrophys.* **434**, 593–598 (2005).
49. Mennella, V., Baratta, G. A., Palumbo, M. E. & Bergin, E. A. Synthesis of CO and CO_2 molecules by UV irradiation of water ice-covered hydrogenated carbon grains. *Astrophys. J.* **643**, 923–931 (2006).
50. Raut, U., Fulvio, D., Loeffler, M. J. & Baragiola, R. A. Radiation synthesis of carbon dioxide in ice-coated carbon: implications for interstellar grains and icy moons. *Astrophys. J.* **752**, 159 (2012).
51. Moore, M. H. & Hudson, R. L. IR detection of H_2O_2 at 80 K in ion-irradiated laboratory ices relevant to Europa. *Icarus* **145**, 282–288 (2000).
52. Gomis, O., Leto, G. & Strazzulla, G. Hydrogen peroxide production by ion irradiation of thin water ice films. *Astron. Astrophys.* **420**, 405–410 (2004).
53. Zheng, W., Jewitt, D. & Kaiser, R. I. Temperature dependence of the formation of hydrogen, oxygen, and hydrogen peroxide in electron-irradiated crystalline water ice. *Astrophys. J.* **648**, 753–761 (2006).
54. Laffon, C., Lacombe, S., Bournel, F. & Parent, P. Radiation effects in water ice: a near-edge x-ray absorption fine structure study. *J. Chem. Phys.* **125**, 204714 (2006).
55. Shi, J., Raut, U., Kim, J. H., Loeffler, M. & Baragiola, R. A. Ultraviolet photon-induced synthesis and trapping of H_2O_2 and O_3 in porous water ice films in the presence of ambient O_2: implications for extraterrestrial ice. *Astrophys. J. Lett.* **738**, L3 (2011).
56. Gladstone, G. R. et al. The atmosphere of Pluto as observed by New Horizons. *Science* **351**, aad8866 (2016).
57. Elliott, H. A. et al. The New Horizons Solar Wind Around Pluto (SWAP) observations of the solar wind from 11-33 au. *Astrophys. J. Suppl. Ser.* **223**, 19 (2016).
58. Grün, E., Horanyi, M. & Sternovsky, Z. The lunar dust environment. *Planet. Space Sci.* **59**, 1672–1680 (2011).
59. Pirronello, V., Brown, W. L., Lanzerotti, L. J., Marcantonio, K. J. & Simmons, E. H. Formaldehyde formation in a H2O/CO2 ice mixture under irradiation by fast ions. *Astrophys. J.* **262**, 636–640 (1982).
60. Gerakines, P. A., Moore, M. H. & Hudson, R. L. Carbonic acid production in H_2O:CO_2 ices. UV photolysis vs. proton bombardment. *Astron. Astrophys.* **357**, 793–800 (2000).
61. Pilling, S. et al. Radiolysis of H_2O:CO_2 ices by heavy energetic cosmic ray analogs. *Astron. Astrophys.* **523**, A77 (2010).
62. Bennett, C. J., Pirim, C. & Orlando, T. M. Space-weathering of solar system bodies: a laboratory perspective. *Chem. Rev.* **113**, 9086–9150 (2013).
63. Famá, M., Loeffler, M. J., Raut, U. & Baragiola, R. A. Radiation-induced amorphization of crystalline ice. *Icarus* **207**, 314–319 (2010).
64. Rathbun, J. A., Rodriguez, N. J. & Spencer, J. R. Galileo PPR observations of Europa: hotspot detection limits and surface thermal properties. *Icarus* **210**, 763–769 (2010).
65. Paranicas, C., Cooper, J. F., Garrett, H. B., Johnson, R. E. & Sturner, S. J. Europa's radiation environment and its effects on the surface. In *Europa* (eds Pappalardo, R. T., McKinnon, W. B. & Khurana, K. K.) 529–544 (University of Arizona Press, 2009).
66. Loeffler, M. J. & Hudson, R. L. Descent without modification? The thermal chemistry of H_2O_2 on Europa and other icy worlds. *Astrobiology* **15**, 453–461 (2015).
67. Bushouse, H. et al. JWST calibration pipeline. *Zenodo* https://zenodo.org/records/8099867 (2023).
68. Bohlin, R. C., Gordon, K. D. & Tremblay, P. E. Techniques and review of absolute flux calibration from the ultraviolet to the mid-infrared. *Publ. Astron. Soc. Pac.* **126**, 711 (2014).
69. Nimmo, F. et al. Mean radius and shape of Pluto and Charon from New Horizons images. *Icarus* **287**, 12–29 (2017).
70. Villanueva, G. L., Smith, M. D., Protopapa, S., Faggi, S. & Mandell, A. M. Planetary Spectrum Generator: an accurate online radiative transfer suite for atmospheres, comets, small bodies and exoplanets. *J. Quant. Spectrosc. Radiat. Transf.* **217**, 86–104 (2018).
71. Villanueva, G. L. et al. *Fundamentals of the Planetary Spectrum Generator* (2022).
72. Hase, F., Wallace, L., McLeod, S. D., Harrison, J. J. & Bernath, P. F. The ACE-FTS atlas of the infrared solar spectrum. *J. Quant. Spectrosc. Radiat. Transf.* **111**, 521–528 (2010).
73. Allodi, M. A. et al. Complementary and emerging techniques for astrophysical ices processed in the laboratory. *Space Sci. Rev.* **180**, 101–175 (2013).
74. Fayolle, M. et al. Testing tholins as analogues of the dark reddish material covering Pluto's Cthulhu region. *Icarus* **367**, 114574 (2021).
75. Markwardt, C. B. Non-linear Least-squares Fitting in IDL with MPFIT. *Astron. Soc. Pacif. Conf. Ser.* **411**, 251–254 (2009).
76. Henyey, L. G. & Greenstein, J. L. Diffuse radiation in the Galaxy. *Astrophys. J.* **93**, 70–83 (1941).
77. Bohren, C. F. & Huffman, D. R. *Absorption and Scattering of Light by Small Particles*. (Wiley-Interscience, 1983).
78. Roser, J. E., Ricca, A., Cartwright, R. J., Dalle Ore, C. & Cruikshank, D. P. The infrared complex refractive index of amorphous ammonia ice at 40 K (1.43–22.73 μm) and its relevance to outer solar system bodies. *Planet. Sci. J.* **2**, 240 (2021).
79. Hudson, R. L., Gerakines, P. A. & Yarnall, Y. Y. Ammonia ices revisited: new IR intensities and optical constants for solid NH_3. *Astrophys. J.* **925**, 156 (2022).
80. de Sanctis, M. C. et al. Bright carbonate deposits as evidence of aqueous alteration on (1) Ceres. *Nature* **536**, 54–57 (2016).
81. Moore, J. M. et al. The geology of Pluto and Charon through the eyes of New Horizons. *Science* **351**, 1284–1293 (2016).
82. Schenk, P. M. et al. Breaking up is hard to do: global cartography and topography of Pluto's mid-sized icy moon Charon from New Horizons. *Icarus* **315**, 124–145 (2018).

Acknowledgements
This work is based on observations made with the NASA/ESA/CSA James Webb Space Telescope. The data were obtained from the Mikulski Archive for Space Telescopes at the Space Telescope Science Institute, which is operated by the Association of Universities for Research in Astronomy, Inc., under NASA contract NAS 5-03127 for JWST. These observations are associated with program #1191. S.P. thanks the NASA grants 80NSSC19K0821 and 80NSSC19K0554 for partial funding that supported her work. W.M.G. thanks the NASA grants 80NSSC19K0821 and 80NSSC19K0556 for partial funding that supported his work. J.S. acknowledges support from Lowell Observatory and Northern Arizona University during his sabbatical stay in Flagstaff, AZ. U.R. was partially supported by NASA grants 80NSSC18K1391 and 80NSSC22K1036. R.B. acknowledges support from the French National Center for Scientific Research (JWST mission).

Author contributions
J.S. and B.H. designed the observations and prepared the observational plans. S.P., U.R., I.W., G.L.V., and J.C. analyzed the data, extracted calibrated spectra, and performed retrievals. U.R. and B.M. performed laboratory spectroscopy experiments on H_2O–CO_2 ice mixtures. S.P., U.R., I.W., J.S., G.L.V., J.C., B.H., W.M.G., R.B, R.J.C., B.M., J.P.E., A.H.P., A.G.-L., N.P.-A., S.N.M., and H.B.H. contributed to the interpretation of the data, the preparation, writing, and editing of the paper.

Competing interests
The authors declare no competing interests.

Additional information
Supplementary information The online version contains supplementary material available at https://doi.org/10.1038/s41467-024-51826-4.

Correspondence and requests for materials should be addressed to Silvia Protopapa.

Peer review information *Nature Communications* thanks the anonymous reviewers for their contribution to the peer review of this work. A peer review file is available.